

# Giant and anisotropic magnetostriction in $\beta$ -O<sub>2</sub> at 110 T

Akihiko Ikeda,<sup>1,\*</sup> Yuya Kubota,<sup>2,†</sup> Yuto Ishii,<sup>3</sup> Xuguang Zhou,<sup>3</sup> Shiyue Peng,<sup>3</sup> Hiroaki Hayashi,<sup>3</sup> Yasuhiro H. Matsuda,<sup>3</sup> Kosuke Noda,<sup>1</sup> Tomoya Tanaka,<sup>1</sup> Kotomi Shimbori,<sup>1</sup> Kenta Seki,<sup>1</sup> Hideaki Kobayashi,<sup>1</sup> Dilip Bhoi,<sup>1</sup> Masaki Gen,<sup>3,4</sup> Kamini Gautam,<sup>4</sup> Mitsuru Akaki,<sup>5</sup> Shiro Kawachi,<sup>6</sup> Shusuke Kasamatsu,<sup>7</sup> Toshihiro Nomura,<sup>8</sup> Yuichi Inubushi,<sup>2,9</sup> and Makina Yabashi<sup>2,9</sup>

<sup>1</sup>Department of Engineering Science, University of Electro-Communications, Chofu, Tokyo 182-8585, Japan

<sup>2</sup>RIKEN SPring-8 Center, Sayo, Hyogo 679-5148, Japan

<sup>3</sup>Institute for Solid State Physics, University of Tokyo, Kashiwa, Chiba 277-8581, Japan

<sup>4</sup>RIKEN Center for Emergent Matter Science (CEMS), Wako 351-0198, Japan

<sup>5</sup>Institute for Material Research, Tohoku University, Sendai, Miyagi 980-0812, Japan

<sup>6</sup>Graduate School of Science, University of Hyogo, Koto, Hyogo 678-1297, Japan

<sup>7</sup>Faculty of Science, Yamagata University, Kojirakawa, Yamagata 990-8560, Japan

<sup>8</sup>Department of Physics, Faculty of Science, Shizuoka University, Shizuoka 422-8529, Japan

<sup>9</sup>Japan Synchrotron Radiation Research Institute (JASRI), Sayo, Hyogo 679-5198, Japan

(Dated: April 15, 2025)

Magnetostriction is a crystal's deformation under magnetic fields, usually in the range of  $10^{-6}$  -  $10^{-3}$ , where the lattice change occurs with the change of spin and orbital state through spin-lattice couplings. In strong magnetic fields beyond 100 T, the significant Zeeman energy competes with the lattice interactions, where one can expect considerable magnetostriction. However, directly observing magnetostriction above 100 T is challenging, because generating magnetic fields beyond 100 T accompanies the destruction of the coil with a single-shot  $\mu$ -second pulse. Here, we observed the giant and anisotropic magnetostriction of  $\sim 1$  % at 110 T in the spin-controlled crystal of  $\beta$ -O<sub>2</sub>, by combining the single-shot diffraction of x-ray free-electron laser (XFEL) and the state-of-the-art portable 100 T generator. The magnetostriction of  $\sim 1$  % is the largest class as a deformation of the unit cell. It is a response of the soft lattice of  $\beta$ -O<sub>2</sub> originating, not only in the competing van der Waals force and exchange interaction, but also the soft state of spin and lattice frustrated on the triangular network. Meanwhile, the anisotropy originates from the strong two-dimensionality of the spin system. Giant magnetostriction in crystals should become more ubiquitous and diverse beyond 100 T, where our XFEL experiment above 100 T opens a novel pathway for their exploration, providing fundamental insights into the roles of spin in stabilizing crystal structures.

Magnetic fields are fertile ground for novel findings in diverse scientific disciplines, ranging from condensed matter physics and planetary science to biological science. The primary objective of applied magnetic fields on materials of a few to a few tens of Teslas are to *see* and *change* the electronic and magnetic states [1, 2], which is constrained by the limited scale of Zeeman energy [3]. On the other hand, magnetic fields beyond  $\sim 100 - 1000$  T are the frontier where they are expected to *break* the crystal state of materials. Zeeman energy at 1000 T amounts to 1340 K, which competes the crystal lattice's energy. Even with a magnetostriction of  $\Delta L/L = 10^{-6}$  at 1 T, the extrapolation with the relation  $\Delta L/L \propto B^2$  gives a significant magnetostriction of 1 % and 100 % at 100 and 1000 T, respectively, making us believe that some drastic change in the relation between spin and lattice happens above 100 T. Meanwhile, the magnetic field can also be a valuable tool to modify the crystal in different ways from other stimuli such as pressure, strain, chemical substitution, and photo-irradiation.

Solid O<sub>2</sub>, a spin-controlled crystal, is the representative candidate for a magnetic field-induced lattice change where the strong spin-lattice coupling is in play [4, 5]. O<sub>2</sub> is a molecular magnet with  $S = 1$  with molecular orbital state  $^3 \Sigma_g^-$  as depicted in Fig. 1(a). Upon cooling, it condenses into a liquid, and then three distinct solids,  $\gamma$ -O<sub>2</sub>,  $\beta$ -O<sub>2</sub>, and  $\alpha$ -O<sub>2</sub>. The variety of the solid phases is the manifestation of the competing interactions in solid O<sub>2</sub> such as van der Waals

interaction, the interaction between the electric quadrupole moments (These two are the origin of exotic phase diagram of solid N<sub>2</sub> [6]), and the antiferromagnetic exchange interactions between the molecular spins as schematically shown in Fig. 1(b). The competing nature in solid O<sub>2</sub> is even more evident in extreme conditions [5]. Under high pressure, three more phases show up, where the phase beyond 100 GPa is a metal with superconducting transition below 0.6 K [7]. Above an ultrahigh magnetic field of 120 T, the ferromagnetic solid O<sub>2</sub>,  $\theta$ -O<sub>2</sub>, is discovered a decade ago as shown in the phase diagram in Fig. 1(c) [8–12].

We work on  $\beta$ -O<sub>2</sub> in the present study because it exhibits softness and fluctuation of lattice and magnetism. The crystal structure of  $\beta$ -O<sub>2</sub> is represented by the triangular lattice in the  $ab$  plane which is stacked in the  $c$  axis. The molecular axis is perpendicular to the  $ab$  plane which is to maximize the exchange interaction between molecular spins by the overlap of  $\pi$  orbitals as schematically shown in Fig. 1(d). The spin interaction is represented by the Heisenberg model with  $S = 1$  on the triangular lattice which suffers from the geometrical frustration, resulting in the suppression of the long-range order and realization of the short-range antiferromagnetic order of  $140^\circ$  structure [13] as schematically drawn in Fig. 1(e). Below 24 K, the lattice shows a first-order structural transition to  $\alpha$ -O<sub>2</sub> with monoclinic structure as shown in Fig. 1(f) where the triangle lattice becomes significantly deformed in the  $ab$

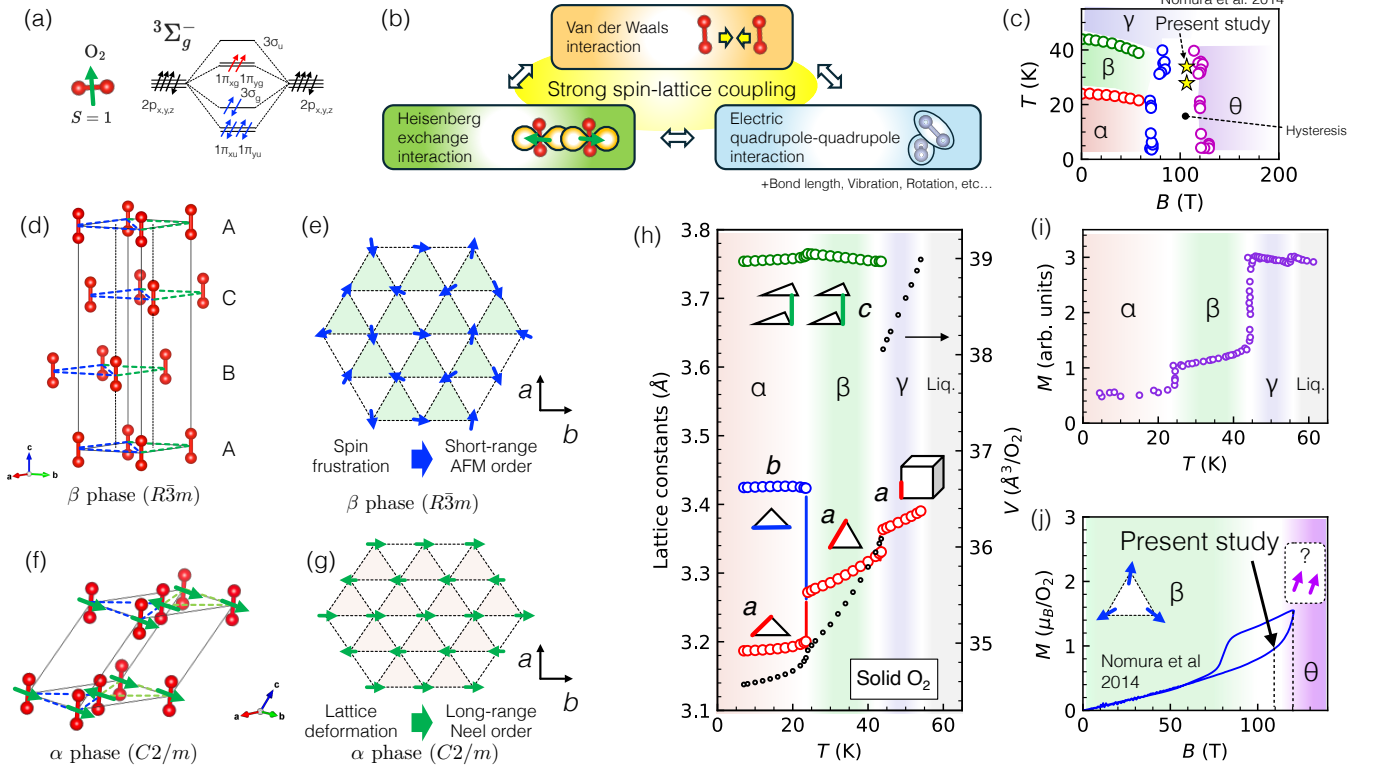


FIG. 1. (a) A schematic drawing for the molecular orbital of  $\text{O}_2$  with  $S = 1$ . (b) A schematic drawing of the determining factors of the structure of solid  $\text{O}_2$  that are competing with each other. (c) A phase diagram of solid  $\text{O}_2$  on a temperature-magnetic field plane reproduced from Ref. [10]. (d) The crystal structure of  $\beta\text{-O}_2$  whose space group is  $R\bar{3}m$ . Layers of a triangular lattice are stacked vertically in the ABC-ABC manner. (e) The schematic of spin configuration on the triangular lattice of  $\beta\text{-O}_2$ . Due to a strong frustration from the lattice symmetry, the spin shows a short-range order with a  $140^\circ$  structure [13]. (f) The crystal structure of  $\alpha\text{-O}_2$  whose space group is  $C2/m$ . It is a deformed structure of  $\beta\text{-O}_2$ . In the layer, the triangle lattice is deformed so that the spin frustration is relaxed. (g) The schematics for the arrangement of the Néel order of spins on the deformed triangular lattice in  $\alpha\text{-O}_2$ , which results in the non-equivalent exchange constant in  $a$  and  $b$  direction. (h) The temperature dependence of lattice parameters and volume in solid  $\text{O}_2$ . The data are taken from Ref. [4]. (i) The temperature dependence of magnetization of solid  $\text{O}_2$ . The data is taken from Ref. [14]. (j) The magnetization of solid  $\text{O}_2$  at 32 K up to 124 T. The data is taken from Ref. [9]. Magnetic field induced phase transition from  $\beta\text{-O}_2$  to  $\theta\text{-O}_2$  occur above 120 T. The present study we generated up to 110 T, where we conducted XRD for the largely strained  $\beta\text{-O}_2$ .

plane. This relaxes the geometrical frustration of the spin system, resulting in the long-range Néel order as shown in Fig. 1(g). The deformation is evident in the lattice constant in Fig. 1(h), showing the splitting of the length of the sides of the triangle by 7 % upon entering the  $\alpha$  phase. Meanwhile, the magnetization data shows a sudden decrease upon entering the  $\alpha$  phase from the  $\beta$  phase, as shown in Fig. 1(i). Surprisingly, the lattice parameter change in the  $ab$  plane in  $\beta\text{-O}_2$  amounts to 2 % in the limited temperature range from 24 to 44 K. In contrast, comparably small changes  $< 0.5$  % are observed in the  $c$  axis in  $\beta\text{-O}_2$  in the same temperature range. This is because the soft triangular lattice is realized by the geometrical frustration of the spin system on the triangular lattice unique to the  $ab$  plane of  $\beta\text{-O}_2$  with the strong spin-lattice coupling, as is also evidenced by the abnormal broadening of x-ray diffraction (XRD) peak with decreasing temperature [15].

When ultrahigh magnetic fields beyond 100 T are applied to that spin-lattice coupled system, we expect drastic changes

in the crystal parameters. Indeed, the ferromagnetic  $\text{O}_2$  is discovered above 120 T whose magnetization data is shown in Fig. 1(j) [8–12], where direct observation of lattice structure change has remain elusive. For this purpose, we realized a method for the macroscopic measurement of  $\Delta L/L$  beyond 100 T using fiber Bragg grating method [16], which has been applied to various systems [17–22] up to 600 T generated using single turn coil method and the electro-magnetic flux compression method [23]. To gain further insights into the spin-lattice coupling above 100 T, one needs the microscopic experimental probes such as XRD besides the macroscopic measurement of  $\Delta L/L$ . However, it is experimentally challenging to perform x-ray diffractometry at 100 T because experimentally obtaining 100 T demands destructive pulse magnets [24]. To overcome this situation, we reported an XRD study with a generation of 77 T pulsed magnetic field by implementing the first Portable INTense Kyokugenjiba (PINK-01) in combination with the single-shot powder diffraction of x-ray free-electron

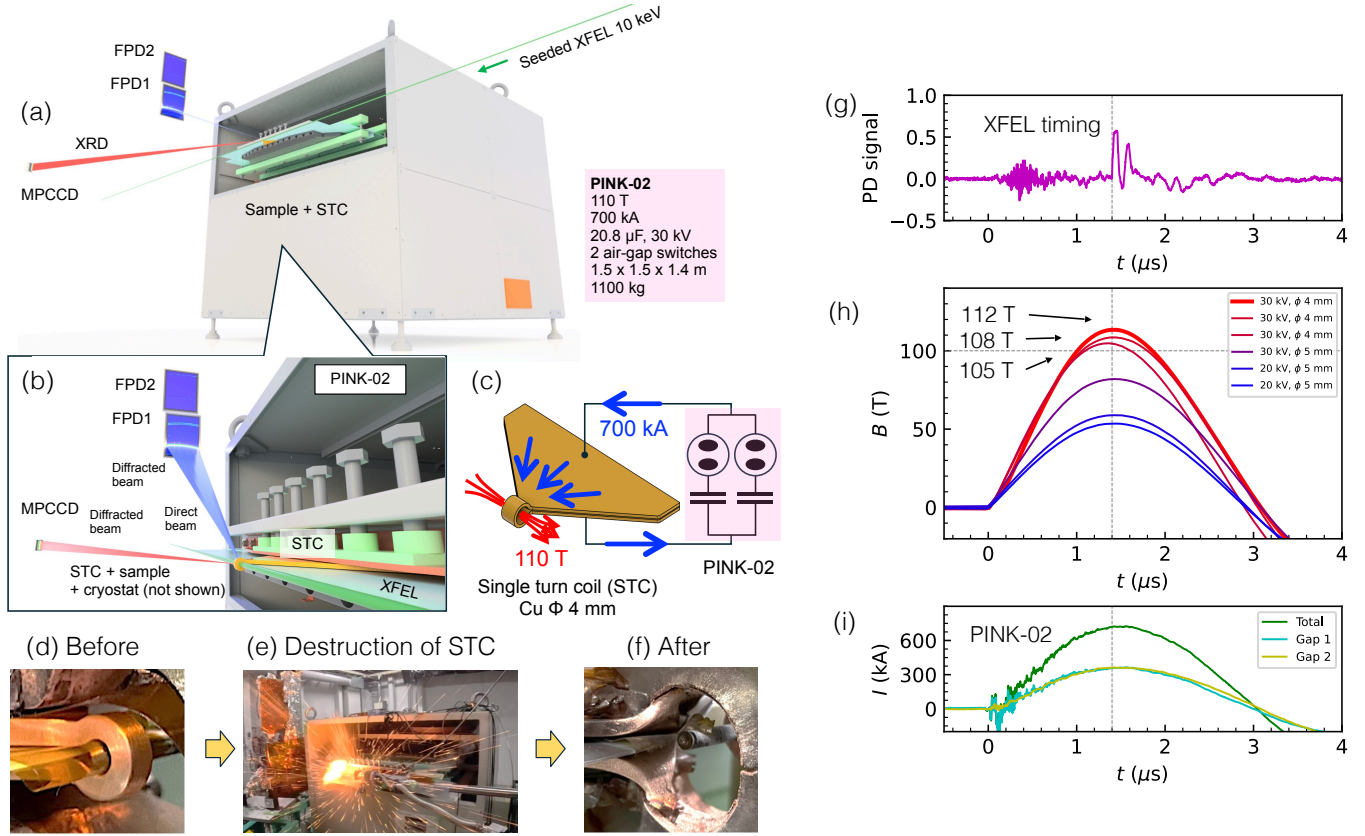


FIG. 2. (a) A schematic view of PINK-02 and the arrangement for the x-ray diffraction in combination with the XFEL, which is installed in SACLA. (b) A magnification at the single turn coil and x-ray beam incident on the sample, with diffracted beams propagating to the x-ray area detectors. (c) A schematic drawing of the electric circuit of PINK-02 and a single-turn coil. (d) A photo of a single turn coil of  $\Phi 4$  mm before the shot. (e) An overview of the single turn coil during the magnetic field generation. (f) A photo of a single turn coil after the shot. (g) X-ray photodiode (PD) signal intensity as a function of time. (h) Representative waveforms of pulsed magnetic field generated using PINK-02 with STCs of  $\phi = 4$  and 5 mm diameter, and charging voltages of 20 and 30 kV. (i) Representative waveforms of the current injected into the STC. There are two switches connected in parallel. Current is measured for each switch. The total current is calculated by taking a sum.

laser (XFEL) from solid sample [25, 26]. Despite the facts, that the proof of principle that the  $\mu$ -second pulse of destructive magnets is compatible with XFEL pulses is achieved, and that the 77 T is the highest field generated by a portable system, the field strength of PINK-01 is not yet enough for the exploration beyond 100 T.

Here, by further refining the technique, we present the portable generation of 110 T using the newly devised PINK-02 in combination with the single shot XRD for  $\beta$ -O<sub>2</sub>. The schematic drawing of the set up is shown in Figs. 2(a) and 2(b). PINK-02 employs two capacitors of 20.8  $\mu$ F in total rated at 30 kV, equipped with a discharge air gap switches as schematically depicted in Fig. 2(c), which weighs 1100 kg. By injecting the high current into the single turn coil, one can obtain the ultrahigh magnetic field, where the STC explodes at each shot, as shown in Figs. 2(d)-(f) and the short movie in Supplemental material. The average magnetic field obtained was  $110 \pm 5$  T with the inner diameter of 4 mm as schematically shown in Fig. 2(h), where the maximum current and voltage are about 700 kA and 30 kV, respectively, as shown in Fig.

2(i). The pulse duration of the magnetic field was 3  $\mu$ s, whose maximum timing is well synchronized with the XFEL pulse as shown in Fig. 2(g).

The results of the powder XRD of  $\beta$ -O<sub>2</sub> obtained at 0 T and 110 T are displayed in the full image of the x-ray detector in Figs. 3(a) and 3(b), respectively. They show three XRD peaks from solid O<sub>2</sub>, 003, 101, 012, by which the solid O<sub>2</sub> is attributed to be in  $\beta$ -O<sub>2</sub>. By comparing the data in Figs. 3(a) and 3(b), one can tell that the peak positions are shifted in the data at 110 T. The shift is qualitatively shown in the plots in Figs. 3(c)-(f), where the sign of the shifts are dependent on the diffraction indexes.

The anisotropic magnetostriction is evidenced by observing the positive shift of 003 diffraction peak and the negative shifts of 101 and 012 at 110 T. In Fig. 3(d), the 003 diffraction peak at 28 K is shown along with that at 35 K, where the scattering angles  $2\theta$  show shifts from  $18.99^\circ$  to  $19.11^\circ$  and from  $18.965^\circ$  to  $19.19^\circ$ , respectively. With the definition  $\Delta d_{hkl}/d_{hkl} \equiv (d_{hkl}^{110\text{ T}}/d_{hkl}^{0\text{ T}}) - 1 = (\sin \theta_{hkl}^{0\text{ T}}/\sin \theta_{hkl}^{110\text{ T}}) - 1$  [27], the values of

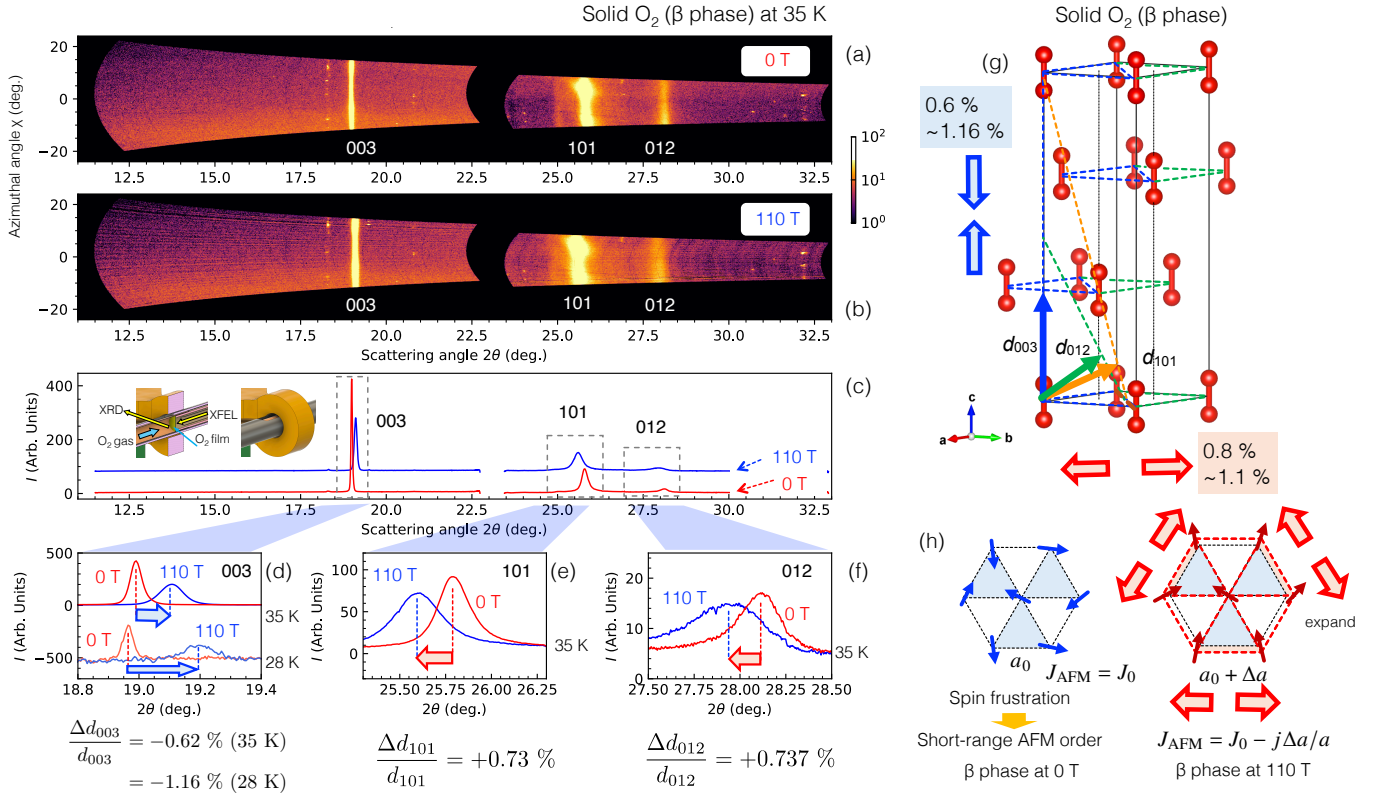


FIG. 3. (a) Powder XRD data from  $\beta$ -O<sub>2</sub> recorded using two-dimensional x-ray detectors at 0 T and (b) at 110 T. (c) Integrated powder XRD data from  $\beta$ -O<sub>2</sub> at 0 T and at 110 T. The inset shows the schematic drawing of the experimental set up at the sample position. (d) The magnified powder XRD data at the 003 reflection of  $\beta$ -O<sub>2</sub> at 35 and 28 K, showing -0.62 and -1.16 % shrinkage of the inter-plane separation at 110 T, respectively. (e) The magnified data of powder XRD at the 101 reflection of  $\beta$ -O<sub>2</sub> at 35 K, showing +0.73 % elongation of the inter-plane separation at 110 T. (f) The magnified data of powder XRD at the 012 reflection of  $\beta$ -O<sub>2</sub> at 35 K, showing +0.737 % elongation of the inter-plane separation at 110 T. (g) The schematic drawing of the crystal structure of  $\beta$ -O<sub>2</sub> with the indication of the shrinkage in the  $c$  axis and elongation in the  $ab$  plane. The diffraction planes are also depicted. (h) The schematic drawing of the crystal structure and spin configuration in  $\beta$ -O<sub>2</sub> at 0 T, where the O<sub>2</sub> molecules form the triangular lattice with the short-range order due to the antiferromagnetic coupling and geometrical frustration. (i) The schematic drawing of the crystal structure and spin configuration in  $\beta$ -O<sub>2</sub> at 110 T, where the spins are more aligned to the external magnetic field, losing the antiferromagnetic short-range order. This results in the expansion of the lattice parameter in  $ab$  plane to relax the antiferromagnetic exchange coupling between spins.

$\Delta d_{003}/d_{003} = -0.62\%$  and  $-1.16\%$  are deduced, respectively, which readily correspond to the shrinkage of the  $c$  axis ( $\Delta c/c < 0$ ) as schematically shown in Fig. 3(g). These are twice the value of the thermally induced change of the  $c$  axis in the  $\beta$  phase as shown in Fig. 1(i), which is only 0.5 %.

In Figs. 3(e) and 3(f), for the 101 and 012 diffraction peaks,  $2\theta$  show shifts from  $25.79^\circ$  to  $25.6^\circ$  and from  $28.12^\circ$  to  $27.91^\circ$ , respectively. The deduced values are  $\Delta d_{101}/d_{101} = +0.73\%$  and  $\Delta d_{012}/d_{012} = +0.737\%$ , respectively. With the pairs of the values  $\Delta d_{hkl}/d_{hkl}$  ( $hkl = 003$  and  $101$ , or  $003$  and  $012$ ), one can deduce the values of  $\Delta a/a = 0.8$ , or  $1.1\%$ , respectively. The reason for the discrepancy in the values is unclear. With an averaged value  $\Delta a/a = 0.95\%$  and  $\Delta c/c = -0.62\%$  at 110 T and 35 K, one can deduce the following values, the volume expansion  $\Delta V/V \equiv \Delta c/c + \Delta a/a \times 2 = 1.28\%$  and the distortion value  $\Delta D/D \equiv \Delta c/c - \Delta a/a = -1.57\%$ . Note that  $\Delta D/D = 0$  if the lattice change is isotropic (i.e.  $\Delta a/a = \Delta c/c$ ). The anisotropic and significant magnetostric-

tion is indicated by the obtained values of  $\Delta a/a = 0.95\%$ ,  $\Delta c/c = -0.62\%$ ,  $\Delta V/V = 1.28\%$ , and  $\Delta D/D = -1.57\%$  in the  $\beta$  phase of solid O<sub>2</sub> at 110 T and 35 K. An even more significant value of  $\Delta c/c = -1.16\%$  at 110 T and 28 K is emphasized.

The anisotropic magnetostriction should originate in the strongly two-dimensional spin system in  $\beta$ -O<sub>2</sub>. To clarify the origin, we consider a Heisenberg Hamiltonian with exchange striction effect as follows,  $\mathcal{H} = \sum_{\langle i,j \rangle} J(\mathbf{R}_{i,j}) \hat{\mathbf{S}}_i \cdot \hat{\mathbf{S}}_j - g\mu_B \sum_i \hat{\mathbf{S}}_i \cdot \mathbf{B}$ , where  $J(\mathbf{R}_{i,j})$ ,  $\langle i,j \rangle$ ,  $\hat{\mathbf{S}}_i$ ,  $g$ ,  $\mu_B$ , and  $\mathbf{B}$  are exchange constant dependent on intermolecular arrangement  $\mathbf{R}_{i,j}$ , pairs of the nearest neighbor sites, spin operator,  $g$ -factor, Bohr magneton, and magnetic field. The first and second terms of the Hamiltonian describe the antiferromagnetic exchange coupling between spins on the nearest neighboring sites of the triangle lattice and the Zeeman energy for individual spins, respectively. For simplicity, we consider that  $J(\mathbf{R}_{i,j})$  depends

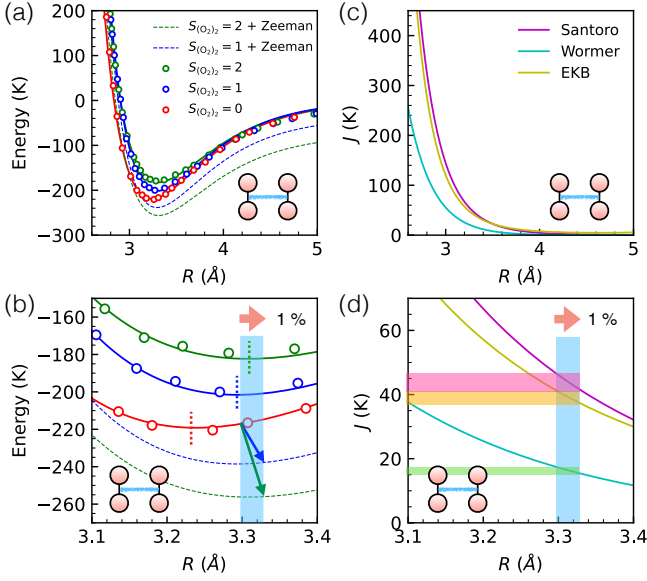


FIG. 4. (a) Intermolecular potential of the dimer  $(\text{O}_2)_2$  in the parallel geometry calculated in Ref. [28] as a function of total spin  $S_{(\text{O}_2)_2} = 0, 1$ , and  $2$ . We plotted the states  $S_{(\text{O}_2)_2} = 1$  and  $S_{(\text{O}_2)_2} = 2$  with the Zeeman effect at 110 T. (b) Magnification of a part of (a). (c) Exchange constant  $J$  of spins between neighboring molecules as a function of  $R$  calculated [29, 30] and deduced from a high pressure study [31]. (d) Magnification of a part of (c).

only on  $\Delta a/a$ . We obtain  $J(a + \Delta a) = J_0 - j\Delta a/a$ , where  $J_0$  and  $j$  are the exchange constant without strain and the coefficient for the strain-dependent change of exchange constant. The Hamiltonian qualitatively explains the lattice expansion in the  $ab$  plane. First, the magnetization gradually increases up to  $0.6 \mu_B/\text{O}_2$  [9], where the Heisenberg term of the Hamiltonian increases the total energy. The system tries to compensate the energy increase by minimizing the exchange constant  $J$ , which is realized by increasing the intermolecular distance in the  $ab$  plane ( $\Delta a/a$ ). The strong contraction in the  $c$  axis is unique because it is much larger than the temperature-induced change. However, the origin is unclear because the inter-layer coupling of spins being considered negligible [4]. One possibility is that the contraction occurs to compensate the sizeable in-plane expansion so that the volume expansion is minimized.

A spin-dependent intermolecular potential calculated for the dimer  $(\text{O}_2)_2$  in parallel geometry shows also qualitative agreement with the above discussion [28]. In Figs. 4(a) and 4(b) shows the intermolecular potential with a variation of  $S_{(\text{O}_2)_2} = 0, 1$ , and  $2$ , where the data points are taken from Ref. [28] and the curves are our fit to the Morse potential  $M(R) = d \left( 1 - (1 - \exp(-(R - R_0)/a))^2 \right)$  with  $d$ ,  $a$ , and  $R_0$  being the depth, the inverted width, and the equilibrium position of the potential, respectively. As shown in Fig. 4(b),  $S_{(\text{O}_2)_2} = 0$  has the lowest energy with the first excited state and the second excited state being  $S_{(\text{O}_2)_2} = 1$  and  $S_{(\text{O}_2)_2} = 2$ , agreeing with the antiferromagnetic spin coupling between

$\text{O}_2$  molecules in parallel geometry. Note also that the value of equilibrated  $R$  increases with increasing  $S_{(\text{O}_2)_2}$  as indicated by the vertical dotted lines. As the dashed lines indicate, the spin triplet and spin quintet state become more stable than the spin singlet state due to the Zeeman effect at 110 T. This trend in the intermolecular potential qualitatively explains the observed trend in the  $\text{O}_2$  crystal. The dependence of the exchange constant  $J$  on the intermolecular distance of  $\text{O}_2$  is estimated by calculations [29, 30] and a high-pressure experiment of solid  $\text{O}_2$  [31] as shown in Figs. 4(c) and 4(d). These all show that  $J$  is decreasing with the increasing  $R$  in good agreement with our model.  $\Delta J/J$  varies from -3 to -5 K/bond depending on the curves in Fig. 4(d), which amounts to -9 to -15 K/ $\text{O}_2$ , which is a sufficient value for the lattice to move for 1 % considering the energy scale in the intermolecular potentials in Figs. 4(a) and 4(b).

The qualitative argument above with the dimer  $(\text{O}_2)_2$  is further strengthened by our first-principles calculation of the exchange constants in the solid  $\beta$  phase. Here, we denote the nearest-neighbor exchange interaction in the  $ab$  plane direction and out-of-plane directions as  $J_1$  and  $J_2$ , respectively. The calculation uses the vdW density functional theory and the tight-binding model calculation. The calculated result of  $J_1(0 \text{ T})$  and  $J_1(110 \text{ T})$  are 47.35 and 41.8 K/bond, where  $\Delta J_1 = -5.55 \text{ K}$  is an 11.8 % reduction of the AFM interaction, being in good agreement with the observed expansion of the lattice constant in the  $ab$  plane with increasing ferromagnetic correlation. The calculated result of  $J_2(0 \text{ T})$  and  $J_2(110 \text{ T})$  are 6.5 and 7.4 K/bond, where  $\Delta J_2 = +0.9 \text{ K}$  is an 14.3 % increase of the AFM interaction.  $\Delta J_2$  is less significant than  $\Delta J_1$  and the sign counters to the observed lattice change, indicating that the shrinkage in  $c$  axis at 110 T is driven by the compensation of the lattice volume expansion due to expanding  $ab$  plane rather than the exchange striction mechanism with  $J_2$ .

The significant magnetostriction may be due to the large fluctuation of the spins on the triangular lattice, which is strongly coupled to the crystal lattice. The temperature-induced lattice change in the  $ab$  plane of  $\beta\text{-O}_2$  is as significant as 2 % with  $\Delta T = 20 \text{ K}$ , indicating that phonon and magnetic contribution to the lattice is crucial in  $\beta\text{-O}_2$ . The uniqueness of the lattice of  $\beta\text{-O}_2$  is highlighted by the fact that the lattice change is much more minor in  $\alpha\text{-O}_2$  where the spins become rigid with the Néel order. The significance of the lattice change is consistent with previous XRD studies on the  $\alpha$  phase of solid  $\text{O}_2$  at 5 T [32] and 28 T [33]. First, a large  $\Delta V/V = 1 \%$  is reported at 5 T at 7 K [32], later confirmed as an extrinsic effect by Ref. [33]. Ref. [33] further put a constraint that  $\Delta d/d < 1 \times 10^{-4}$  at 5 T and  $\Delta d/d < 2 \times 10^{-3}$  at 25 T. If we assume the quadratic dependence  $\Delta d/d \approx pB^2$  with typical values of  $\Delta d/d = 1 \%$  and  $B = 100 \text{ T}$ , we obtain  $\Delta d/d \approx 2.5 \times 10^{-5}$  at 5 T,  $6.3 \times 10^{-4}$  at 25 T by an interpolation, which are consistent with the previous XRD study up to 28 T [33] and the present result.

The present lattice change occurs in the unit cell without phase transition, which is considered the greatest ever reported to our best knowledge. Larger magnetostrictions are observed

in Heusler alloy [34] and manganite systems [35], where the domain's reorientation and the phase transition are the sources of the significant lattice change. Lastly, we should observe the complete lattice transformation to  $\theta$ -O<sub>2</sub> [8] above 120 T. The clarification of the crystal structure of  $\theta$ -O<sub>2</sub> is, without a doubt, the most crucial goal of our study to follow. We are currently evaluating methods to increase the maximum magnetic field that PINK-02 generates.

A fruitful discussion with J. Nasu is acknowledged. The experiment was carried out with the approval of JASRI (Proposal No. 2024A8010 and 2024B8046). The authors would like to acknowledge the support from the technical staff of the SACLA facility. They also appreciate the support from the SACLA/SPRING-8 Basic Development Program (2021 - 2024). This work is partially supported by JST FOREST program No. JPMJFR222W and No. JPMJFR2037, JSPS Grant-in-Aid for Scientific Research on Innovative Areas (A) (1000 T Science) 23H04861, 23H04859, 24H01633, and Grant-in-Aid for Scientific Research (B) 23H01121, and Grant-in-Aid for Scientific Research 24K21043, and MEXT LEADER program No. JPMXS0320210021.

\* These authors contributed equally to this work: [a-ikeda@uec.ac.jp](mailto:a-ikeda@uec.ac.jp)

† These authors contributed equally to this work: [kubota@spring8.or.jp](mailto:kubota@spring8.or.jp)

- [1] S. Gerber, H. Jang, H. Nojiri, S. Matsuzawa, H. Yasumura, D. A. Bonn, R. Liang, W. N. Hardy, Z. Islam, A. Mehta, S. Song, M. Sikorski, D. Stefanescu, Y. Feng, S. A. Kivelson, T. P. Devereaux, Z. X. Shen, C. C. Kao, W. S. Lee, D. Zhu, and J. S. Lee, Three-dimensional charge density wave order in YBa<sub>2</sub>Cu<sub>3</sub>O<sub>6.67</sub> at high magnetic fields, *Science* **350**, 949 (2015).
- [2] S. Ran, I.-L. Liu, Y. S. Eo, D. J. Campbell, P. M. Neves, W. T. Fuhrman, S. R. Saha, C. Eckberg, H. Kim, D. Graf, F. Balakirev, J. Singleton, J. Paglione, and N. P. Butch, Extreme magnetic field-boosted superconductivity, *Nat. Phys.* **15**, 1250 (2019).
- [3] Zeeman energy mounts to over 1.34 K for a free-electron spin at 1 T with the relation  $E_{\text{Zeeman}} = g\mu_B S_z B_z$ .  $g$ ,  $\mu_B$ ,  $S_z$ , and  $B_z$  are  $g$ -factor, Bohr magneton, Spin, and external magnetic field, respectively.
- [4] Y. A. Freiman and H. J. Jodl, Solid oxygen, *Phys. Rep.* **401**, 1 (2004).
- [5] Y. A. Freiman, H. J. Jodl, and Y. Crespo, Solid oxygen revisited, *Phys. Rep.* **743**, 1 (2018).
- [6] M. Kirszt, C. G. Pruteanu, P. I. C. Cooke, and G. J. Ackland, Understanding solid nitrogen through molecular dynamics simulations with a machine-learning potential, *Phys. Rev. B* **110**, 184107 (2024).
- [7] K. Shimizu, K. Suhara, M. Ikumo, M. I. Erements, and K. Amaya, Superconductivity in oxygen, *Nature* **393**, 767 (1998).
- [8] T. Nomura, Y. H. Matsuda, S. Takeyama, A. Matsuo, K. Kindo, J. L. Her, and T. C. Kobayashi, Novel Phase of Solid Oxygen Induced by Ultrahigh Magnetic Fields, *Phys. Rev. Lett.* **112**, 247201 (2014).
- [9] T. Nomura, Y. H. Matsuda, S. Takeyama, A. Matsuo, K. Kindo, and T. C. Kobayashi, Phase boundary of  $\theta$  phase of solid oxygen in ultrahigh magnetic fields, *Phys. Rev. B* **92**, 064109 (2015).
- [10] T. Nomura, Y. H. Matsuda, and T. C. Kobayashi, H-T phase diagram of solid oxygen, *Phys. Rev. B* **96**, 054439 (2017).
- [11] T. Nomura, Y. Kohama, Y. H. Matsuda, K. Kindo, and T. C. Kobayashi,  $\alpha$ - $\beta$  and  $\beta$ - $\gamma$  phase boundaries of solid oxygen observed by adiabatic magnetocaloric effect, *Phys. Rev. B* **95**, 104420 (2017).
- [12] T. Nomura, Y. H. Matsuda, and T. C. Kobayashi, Solid and liquid oxygen under ultrahigh magnetic fields, *Oxygen* **2**, 152 (2022).
- [13] F. Dunstetter, V. P. Plakhti, and J. Schweizer, The magnetic structure of  $\beta$  oxygen: A neutron polarisation analysis study, *J. Magn. Magn. Mater.* **72**, 258 (1988).
- [14] R. J. Meier, C. J. Schinkel, and A. d. Visser, Magnetisation of condensed oxygen under high pressures and in strong magnetic fields, *J. Phys. C: Solid State Phys.* **15**, 1015 (1982).
- [15] A. S. Baryl'nik and A. I. Prokhvatilov, Spontaneous magnetostriction effects in  $\alpha$ - and  $\beta$ -phases of oxygen, *Low Temp. Phys.* **20**, 716 (1994).
- [16] A. Ikeda, T. Nomura, Y. H. Matsuda, S. Tani, Y. Kobayashi, H. Watanabe, and K. Sato, High-speed 100 MHz strain monitor using fiber Bragg grating and optical filter for magnetostriction measurements under ultrahigh magnetic fields, *Rev. Sci. Instrum.* **88**, 083906 (2017).
- [17] A. Ikeda, Y. H. Matsuda, K. Sato, and J. Nasu, A Review on Magnetic Field Induced Spin Crossover in LaCoO<sub>3</sub> up to 600 T, *J. Phys. Soc. Jpn.* **93**, 121005 (2024).
- [18] A. Ikeda, Y. H. Matsuda, and K. Sato, Two Spin-State Crystalizations in LaCoO<sub>3</sub>, *Phys. Rev. Lett.* **125**, 177202 (2020).
- [19] T. Nomura, A. Ikeda, M. Gen, A. Matsuo, K. Kindo, Y. Kohama, Y. H. Matsuda, S. Zherlitsyn, J. Wosnitza, H. Tsuda, and T. C. Kobayashi, Physical properties of liquid oxygen under ultrahigh magnetic fields, *Phys. Rev. B* **104**, 224423 (2021).
- [20] A. Ikeda, Y. H. Matsuda, K. Sato, Y. Ishii, H. Sawabe, D. Nakamura, S. Takeyama, and J. Nasu, Signature of spin-triplet exciton condensations in LaCoO<sub>3</sub> at ultrahigh magnetic fields up to 600 T, *Nat. Commun.* **14**, 1744 (2023).
- [21] T. Nomura, P. Corboz, A. Miyata, S. Zherlitsyn, Y. Ishii, Y. Kohama, Y. H. Matsuda, A. Ikeda, C. Zhong, H. Kageyama, and F. Mila, Unveiling new quantum phases in the Shastry-Sutherland compound SrCu<sub>2</sub>(BO<sub>3</sub>)<sub>2</sub> up to the saturation magnetic field, *Nat. Commun.* **14**, 3769 (2023).
- [22] M. Gen, A. Ikeda, K. Aoyama, H. O. Jeschke, Y. Ishii, H. Ishikawa, T. Yajima, Y. Okamoto, X. Zhou, D. Nakamura, S. Takeyama, K. Kindo, Y. H. Matsuda, and Y. Kohama, Signatures of a magnetic superstructure phase induced by ultrahigh magnetic fields in a breathing pyrochlore antiferromagnet, *Proc. Natl. Acad. Sci. U.S.A.* **120**, e2302756120 (2023).
- [23] D. Nakamura, A. Ikeda, H. Sawabe, Y. H. Matsuda, and S. Takeyama, Record indoor magnetic field of 1200 T generated by electromagnetic flux-compression, *Rev. Sci. Instrum.* **89**, 095106 (2018).
- [24] F. Herlach, Pulsed magnets, *Rep. Prog. Phys.* **62**, 859 (1999).
- [25] A. Ikeda, Y. H. Matsuda, X. Zhou, S. Peng, Y. Ishii, T. Yajima, Y. Kubota, I. Inoue, Y. Inubushi, K. Tono, and M. Yabashi, Generating 77 T using a portable pulse magnet for single-shot quantum beam experiments, *Appl. Phys. Lett.* **120**, 142403 (2022).
- [26] A. Ikeda, Y. H. Matsuda, X. Zhou, T. Yajima, Y. Kubota, K. Tono, and M. Yabashi, Single shot x-ray diffractometry in SACLA with pulsed magnetic fields up to 16 T, *Phys. Rev. Research* **2**, 043175 (2020).
- [27] Deduced from the following relation,  $\lambda = 2d_{hkl}^{0\text{ T}} \sin\left(\theta_{hkl}^{0\text{ T}}\right) = 2d_{hkl}^{110\text{ T}} \sin\left(\theta_{hkl}^{110\text{ T}}\right)$ .
- [28] B. Bussery and P. E. S. Wormer, A van der Waals intermolecular

- potential for (O<sub>2</sub>)<sub>2</sub>, *J. Chem. Phys.* **99**, 1230 (1993).
- [29] R. D. Eters, K. Kobashi, and J. Belak, Calculated properties of solid O<sub>2</sub> under pressure at low temperature, *Phys. Rev. B* **32**, 4097 (1985).
- [30] R. LeSar and R. D. Eters, Character of the  $\alpha$ - $\beta$  phase transition in solid oxygen, *Phys. Rev. B* **37**, 5364 (1988).
- [31] M. Santoro, F. A. Gorelli, L. Ulivi, R. Bini, and H. J. Jodl, Antiferromagnetism in the high-pressure phases of solid oxygen: Low-energy electronic transitions, *Phys. Rev. B* **64**, 064428 (2001).
- [32] K. Katsumata, S. Kimura, U. Staub, Y. Narumi, Y. Tanaka, S. Shimomura, T. Nakamura, S. W. Lovesey, T. Ishikawa, and H. Kitamura, The giant magneto-volume effect in solid oxygen, *J. Phys.: Condens. Matter* **17**, L235 (2005).
- [33] Y. H. Matsuda, A. Shimizu, A. Ikeda, T. Nomura, T. Yajima, T. Inami, K. Takahashi, and T. C. Kobayashi, High magnetic field x-ray diffraction study of the  $\alpha$  phase of solid oxygen: Absence of giant magnetostriction, *Phys. Rev. B* **100**, 214105 (2019).
- [34] T. Kakeshita and K. Ullakko, Giant magnetostriction in ferromagnetic shape-memory alloys, *MRS Bulletin* **27**, 105 (2002).
- [35] Y. Tokura, Critical features of colossal magnetoresistive manganites, *Rep. Prog. Phys.* **69**, 797 (2006).
- [36] T. Ishikawa, H. Aoyagi, T. Asaka, Y. Asano, N. Azumi, T. Bizen, H. Ego, K. Fukami, T. Fukui, Y. Furukawa, S. Goto, H. Hanaki, T. Hara, T. Hasegawa, T. Hatsui, A. Higashiya, T. Hirono, N. Hosoda, M. Ishii, T. Inagaki, Y. Inubushi, T. Itoga, Y. Joti, M. Kago, T. Kameshima, H. Kimura, Y. Kirihara, A. Kiyomichi, T. Kobayashi, C. Kondo, T. Kudo, H. Maesaka, X. M. Maréchal, T. Masuda, S. Matsubara, T. Matsumoto, T. Matsushita, S. Matsui, M. Nagasono, N. Nariyama, H. Ohashi, T. Ohata, T. Ohshima, S. Ono, Y. Otake, C. Saji, T. Sakurai, T. Sato, K. Sawada, T. Seike, K. Shirasawa, T. Sugimoto, S. Suzuki, S. Takahashi, H. Takebe, K. Takeshita, K. Tamasaku, H. Tanaka, R. Tanaka, T. Tanaka, T. Togashi, K. Togawa, A. Tokuhisa, H. Tomizawa, K. Tono, S. Wu, M. Yabashi, M. Yamaga, A. Yamashita, K. Yanagida, C. Zhang, T. Shintake, H. Kitamura, and N. Kumagai, A compact X-ray free-electron laser emitting in the sub-ångström region, *Nat. Photonics* **6**, 540 (2012).
- [37] I. Inoue, T. Osaka, T. Hara, T. Tanaka, T. Inagaki, T. Fukui, S. Goto, Y. Inubushi, H. Kimura, R. Kinjo, H. Ohashi, K. Togawa, K. Tono, M. Yamaga, H. Tanaka, T. Ishikawa, and M. Yabashi, Generation of narrow-band x-ray free-electron laser via reflection self-seeding, *Nat. Photonics* **13**, 319 (2019).
- [38] T. Kameshima, S. Ono, T. Kudo, K. Ozaki, Y. Kirihara, K. Kobayashi, Y. Inubushi, M. Yabashi, T. Horigome, A. Holland, K. Holland, D. Burt, H. Murao, and T. Hatsui, Development of an x-ray pixel detector with multi-port charge-coupled device for x-ray free-electron laser experiments, *Rev. Sci. Instrum.* **85**, 033110 (2014).
- [39] G. Kresse and J. Furthmüller, Efficient iterative schemes for ab initio total-energy calculations using a plane-wave basis set, *Phys. Rev. B* **54**, 11169 (1996).
- [40] G. Pizzi, V. Vitale, R. Arita, S. Blügel, F. Freimuth, G. Géranton, M. Gibertini, D. Gresch, C. Johnson, T. Koretsune, J. Ibañez Azpiroz, H. Lee, J.-M. Lihm, D. Marchand, A. Marrazzo, Y. Mokrousov, J. I. Mustafa, Y. Nohara, Y. Nomura, L. Paulatto, S. Poncé, T. Ponweiser, J. Qiao, F. Thöle, S. S. Tsirkin, M. Wierzbowska, N. Marzari, D. Vanderbilt, I. Souza, A. A. Mostofi, and J. R. Yates, Wannier90 as a community code: new features and applications, *J. Phys.: Condens. Matter* **32**, 165902 (2020).
- [41] X. He, N. Helbig, M. J. Verstraete, and E. Bousquet, Tb2j: A python package for computing magnetic interaction parameters, *Comput. Phys. Commun.* **264**, 107938 (2021).
- [42] J. Klimeš, D. R. Bowler, and A. Michaelides, Van der Waals density functionals applied to solids, *Phys. Rev. B* **83**, 195131 (2011), 1102.1358.
- [43] S. L. Dudarev, S. Y. Savrasov, C. J. Humphreys, and a. P. Sutton, Electron-energy-loss spectra and the structural stability of nickel oxide: An LSDA+U study, *Phys. Rev. B* **57**, 1505 (1998).
- [44] S. Kasamatsu, T. Kato, and O. Sugino, First-principles description of van der Waals bonded spin-polarized systems using the vdW-DF+ U method: Application to solid oxygen at low pressure, *Phys. Rev. B* **95**, 235120 (2017).
- [45] J. Kieffer and D. Karkoulis, PyFAI, a versatile library for azimuthal regrouping, *J. Phys.: Conf. Ser.* **425**, 202012 (2013).
- [46] K. Momma and F. Izumi, VESTA3 for three-dimensional visualization of crystal, volumetric, and morphology data, *J. Appl. Crystallogr.* **44**, 1272 (2011).

## METHODS

The experiment was carried out on the beamline 3 (BL3) at SACLA. The pulses of x-ray free-electron laser of SACLA [36] at 10 keV with self-seeding [37] with a dispersion of  $1 \sim 3$  eV is delivered to the powder sample with the mean energy of  $360 \mu\text{J}/\text{pulse}$ .

The all-plastic He-flow micro-cryostat is newly devised for the present purpose of cooling the sample at the coil center down to 10 K, allowing the incident x-ray beam of  $\phi \sim 0.3$  mm to hit the sample, whose overview and a photo are shown in Figs. 5(a) and 5(b). As shown in the detailed view in Fig. 5(c), the diffracted beam escapes from the cryostat with a wide range of scattering angle  $2\theta$  from  $0^\circ$  to  $45^\circ$ . The outer diameter of the micro-cryostat is  $\phi 2.6$  mm, which is held in the vacuum tube of  $\phi 3.6$  mm sitting at the center of the STC with the inner diameter  $\phi 4$  mm, which are schematically depicted in Fig. 5(c). Micro-cryostat is made of fiber-reinforced plastic and the glue SK-229 (Nitto). The vacuum tube and the micro-cryostat are held by the 3D printed vacuum chamber made of the PLA plastic and an inner-coating with the glue SK-229 (Nitto).

The solid  $\text{O}_2$  sample is condensed as a film in situ at the center of STC. As shown in the inset of Fig. 3(c), our micro-cryostat is further modified for the  $\text{O}_2$  sample, where the  $\text{O}_2$  gas inlet is directly connected onto the cold-head of the cryostat. The vacuum tube is also elongated to the direction of the beam downstream, where the hole is machined and covered with Kapton film ( $t = 50 \mu\text{m}$ ) so that the diffracted x-ray can escape. First, we cool the micro-cryostat while we keep the  $\text{O}_2$  gas inlet in vacuum. Next, we introduce  $\text{O}_2$  gas for a limited amount, that is condensed onto the cold-head of the micro-cryostat, and then we evacuate the  $\text{O}_2$  gas inlet to the vacuum again. We can observe the XRD from the sample. We deduced the sample temperature from the XRD to be 28 or 35 K with no lower temperature, which is higher than that with the pre-prepared solid state sample where the sample can be cooled to 10 K. It is may be because the additionally installed  $\text{O}_2$  gas inlet works as a heat source.

The diffracted beam is detected using two kinds of two-dimensional detectors of multi-port charge-coupled device (MPCCD) [38] with a distance of 1.5 m and a pair of flat panel detectors (FPD) with a distance of 1.0 m from the sample. Data are taken with a single shot with no accumulation. Three x-ray images are recorded sequentially at  $t = -0.1, 0$ , and  $0.1$  ms with  $t = 0$  ms being at the maximum magnetic field. In the present experiment, the data of MPCCD is not used. The data after the magnetic field pulse is not obtained for FPD.

The first-principles calculation of the exchange constants between the molecular spins of  $\text{O}_2$  in solid  $\text{O}_2$  was performed using VASP [39] in combination with Wannier90 [40] and TB2J [41] packages. First, VASP is used to obtain the electronic structure of  $\beta$  phase oxygen using the vdW-DF-optB86b functional [42] in combination with a Hubbard- $U$  correction [43] of  $U_{\text{eff}} = 12$  eV, which resulted in a good description of

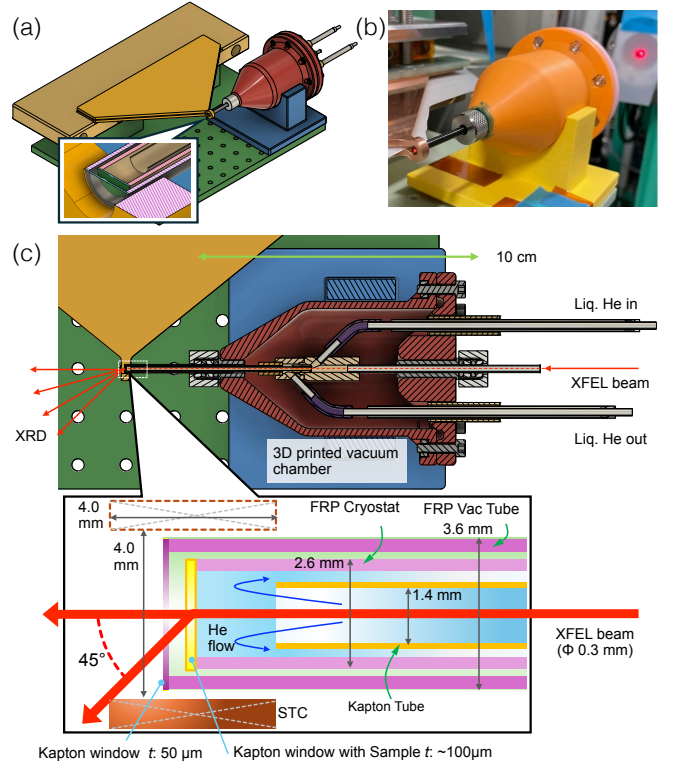


FIG. 5. (a) Overview of the micro-cryostat, 3D printed vacuum chamber, and the STC set up. (b) A photo of the micro-cryostat, the STC and the 3D printed vacuum chamber. (c) Detailed cross-sectional view of the micro-cryostat, 3D printed vacuum chamber and the STC.

the  $\alpha$  phase of solid oxygen in a previous work [44]. The lattice constants were fixed to those determined experimentally in this work, the O-O bond length was fixed to  $1.207 \text{ \AA}$ , and the spin configuration was fixed to the ferromagnetic one. The unit cell in the monoclinic setting was employed with a  $5 \times 6 \times 5$   $k$ -point mesh and a plane wave cutoff energy of 1500 eV. Wannier90 was used to obtain Wannier functions and build a tight-binding model with initial projections on the  $p_x$  and  $p_y$  orbitals of O atoms for  $\pi$  and  $\pi^*$  bands and  $s$  orbitals placed at O-O bond centers for the  $\sigma$  bonding band. Only the  $\pi$  and  $\pi^*$  bands contribute to the spin interactions. The resulting tight-binding model was fed into TB2J code, which uses the Liechtenstein formalism to calculate Heisenberg exchange constants.

The obtained image is analyzed using a python package pyFAI [45]. The crystal structures are rendered using the 3D visualization tool VESTA [46].

**SUPPLEMENTARY VIDEO**

Please see the supplementary video of PINK-02 generating 110 T at BL3 in SACLA 13 times successfully in a row (37 seconds). The same video is also uploaded to [YouTube](#).